Scalable and controllable synthesis of atomic metal electrocatalysts assisted by an egg-box in alginate

Zhang, Lijie; Liu, Tongchao; Chen, Ning; Jia, Yi; Cai, Rongsheng; Theis, Wolfgang; Yang, Xianfeng; Xia, Yanzhi; Yang, Dongjiang; Yao, Xiangdong

DOI:
10.1039/C8TA07469K

Document Version
Peer reviewed version

Journal Name

COMMUNICATION

Scalable and Controllable Synthesis of Atomic Metal Electrocatalysts Assisted by Egg-Box in Alginate

Received 00th January 20xx,
Accepted 00th January 20xx

DOI: 10.1039/x0xx00000x

www.rsc.org/

Lijie Zhang,[a] Tongchao Liu,[b] Ning Chen,[c] Yi Jia,[d] Rongsheng Cai,[e] Wolfgang Theis,[e] Xianfeng Yang,[f] Yanzhi Xia,[a] Dongjiang Yang[a,d,*] and Xiangdong Yao[d,*]

Herein, a general strategy is developed to synthesize atomic metal catalysts using sustainable and earth-abundant sodium alginate (Na-Alg), a common seaweed extract, as a precursor. The "egg-box" structure in Na-Alg after ion-exchange with metal cations (Zn^{2+}, Co^{2+}, Ni^{2+}, Cu^{2+} etc) is the key to achieve the scalable and controllable synthesis of highly dispersed atomic metals. For instance, the atomic Co, Ni and Cu have been successfully synthesized using this method. As a representative, the as synthesized atomically dispersed Co on reduced graphene oxides (A-Co/r-GOs) can reach a maximum metal loading of 3.6 wt.%, showing outstanding catalytic activity and stability for oxygen reduction reaction (ORR) with a half-wave potential ($E_{1/2}$) of 0.842 V vs. RHE that is more positive than that of 20 wt% Pt/C (0.827 V vs. RHE) in alkaline. The A-Co/r-GOs catalyzed zinc-air batteries (ZABs) outperform Pt/C-based ZABs in aspects of discharge voltage and specific zinc capacity, and can work robustly for more than 250 h with negligible voltage loss with refueling the Zn anode and KOH electrolyte periodically. This work opens up a new strategy for general, practical and scalable synthesis of atomic metal catalysts at very low cost.

Recently, the so-called single atom catalysts (SACs) have been regarded as a new research frontier and attracted extensive attentions.[1] Despite of the vague understanding of SACs, such materials with atomic dispersion have exhibited great application potentials in many catalytic fields, such as thermalcatalytic reaction[2, 3], photocatalytic reaction[4, 5], organic conversion[6-9], and electrocatalytic reaction[10, 11]. Especially, given that most of the best electrocatalysts are expensive and scarce precious metals, e.g. Pt for oxygen reduction reaction (ORR)[12], atomically dispersed eletrocatalyst is of great significance in developing alternative electrocatalysts with high efficiency and low cost, such as atomic transition metal (Co[13], Fe[14] etc.) species. It is understood that precise control of electrocatalytic active sites at the atomic level can maximize the metal atom utilization, improving the specific activity per metal atom, thus decreasing ultimately the metal usage[15]. Moreover, the specific electronic structure at active sites induced from charge transfer between atomic metals and supports, can greatly affect the selectivity, catalytic activity and stability.[11, 16-18]

Although many achievements have been made, the synthesis of such atomically dispersed catalysts remains a key challenge because atomic metals are very easy to aggregate to small clusters/nanoparticles (NPs). Traditional strategy to tackle this problem is keeping the metal loading at extremely low level (< 0.5 wt. %) to avoid aggregation.[19] However, the low metal loading limits their catalytic performances in applications.[20] To date, advanced synthetic methods, such as mass-selected soft-landing[21], arc-discharge method[22], atomic layer deposition[23], and derivatives from metal organic frameworks (MOFs) carbonization[13, 24, 25] have been applied to synthesize atomically dispersed catalysts. Nevertheless, it is noticed that all these methods have a common drawback, using complicated synthesis procedure, and/or expensive precursors and low yield. Thus, it is not suitable for scale-up implement in commercialization due to the high cost (even without notable metals) and limited production ability (generally in mg level). Much recently, acid etching of metal/carbon composite was developed to obtain carbon anchored atomic metals.[14, 26] However, the metal nanoparticles (NPs) are often encapsulated by graphitic carbon layers, forming dense core-shell structure, thus protecting the NPs from acid washing, thus it is highly

[a] School of Environmental Science and Engineering; Collaborative Innovation Center for Marine Biomass Fibers, Materials and Textiles of Shandong Province, Qingdao University, Qingdao 266071, P. R. China.
E-mail: d.yang@qdu.edu.cn
[b] School of Advanced Materials, Peking University, Shenzhen Graduate School, Shenzhen 518055, P. R. China.
[c] Canadian Light Source, Saskatoon S7N 0X4, Canada.
[d] Queensland Micro- and Nanotechnology Centre and School of Natural Sciences, Griffith University, Nathan, Brisbane, QLD 4111, Australia
E-mail: x.yao@griffith.edu.au
[e] Nanoscale Physics Research Laboratory School of Physics and Astronomy, University of Birmingham, Birmingham, B15 2TT, UK
[f] Analytical and Testing Centre, South China University of Technology Guangzhou 510640, P. R. China
Electronic Supplementary Information (ESI) available.
See DOI: 10.1039/x0xx00000x

impossible to obtain a fully atomic metal catalyst.[27-30] Accordingly, it is necessary to generate porous channels in the graphitic carbon layers to enable acid accessible to those encapsulated metal NPs. This idea has been confirmed feasible by electrochemical activation[31], but the activation process is very time-consumable. As a consequence, a simple method with highly massive production of atomic metal catalysts is highly demanded. Recently, Zhao *et al.* developed a defect-driven ORR electrocatalyst by carbonization of a Zn-containing metal-organic frameworks (MOFs) over 900 °C, with the evaporation of Zn to create micro-pores and defects.[32] It actually provides an easy and general way to fabricate pores/channels through Zn evaporation. In addition, the generated defects by the Zn evaporation offer enormous active sites to trap the atomic metal atoms,[33, 34] which makes a high loading of atomic metal material available.

Herein, a general strategy to scalable and controllable synthesis of atomically dispersed metal catalysts was proposed by using sustainable sodium alginate (Na-Alg) as a precursor. As seaweed extract, the earth-abundant Na-Alg meets the requirement for scalable and cost-effective synthesis.[35-37] More importantly, Na-Alg could immobilize and disperse targeted metal ions (M^{n+} = Zn^{2+}, Co^{2+}, Ni^{2+}, Cu^{2+} etc.) by forming a special "egg-box" structure.[28, 38-42] This feature enables controllable generation of porous channels and defects in carbon shell after high temperature pyrolysis by facile tuning of molar ratio of Zn and other metals. As a representative, atomic cobalt dispersed on reduced graphene oxides (A-Co/r-GOs) with maximum loading of 3.6 wt. % will be investigated in details in this research. The confined Zn^{2+} and Co^{2+} in "egg-box" synergistically contributed to the formation of atomically dispersed Co after pyrolysis with melamine in nitrogen gas and subsequent acid etching. The detailed structure of single Co site is identified as CoN_3C moiety enclosed in a graphene plane with two axial oxygen molecules absorbed end-on. The as-obtained A-Co/r-GOs catalyst exhibits outstanding catalytic activities for ORR with a half-wave potential ($E_{1/2}$) of 0.842 V vs. RHE in 0.1 M KOH, which is 15 mV more positive than that of 20 wt% Pt/C ($E_{1/2}$ = 0.827 V vs. RHE). The high ORR activity of A-Co/r-GOs can efficiently improve the low efficiency of air cathode for zinc-air batteries (ZABs), thus enhancing the battery performance. As expected, the A-Co/r-GOs-based ZABs show better battery performances than that of Pt/C-based ZABs in aspects of discharge voltage and specific zinc capacity. With refueling the Zn anode and KOH electrolyte by interval of ~ 50 h, the battery can work robustly for more than 250 h with negligible voltage loss. It is worth noting that, as a general synthesis strategy, this method could be also used to produce other atomically dispersed metals such as Ni and Cu.

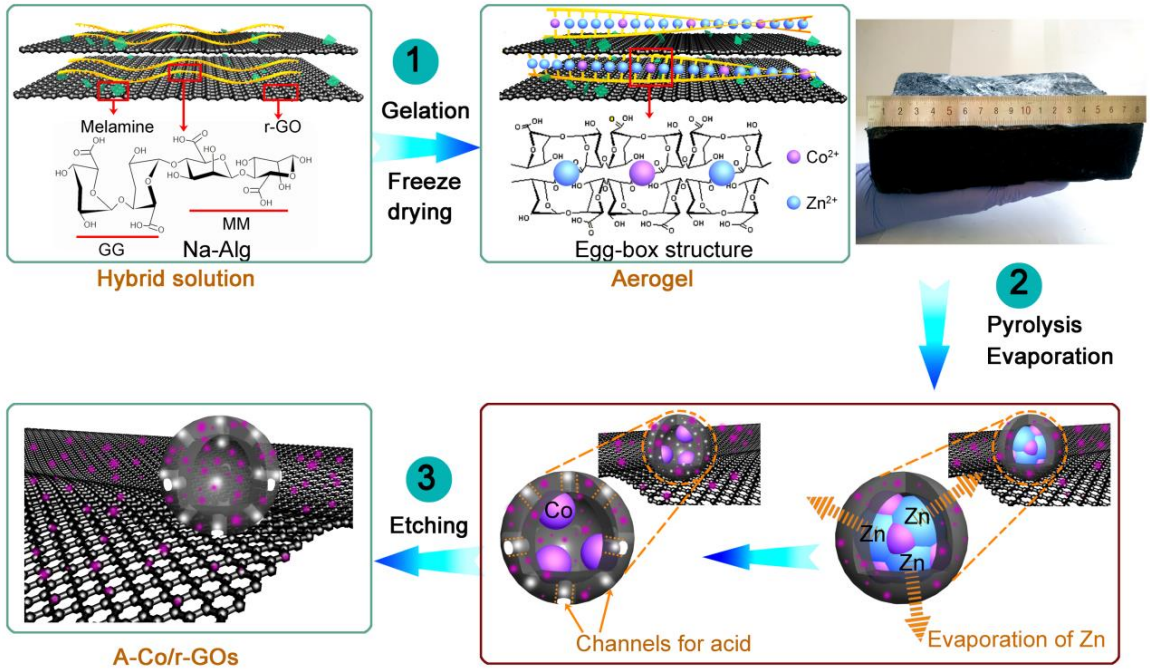

Scheme 1. The formation of A-Co/r-GOs with the assistance of "egg-box" in alginate.

The preparation procedure and formation mechanism of A-Co/r-GOs are shown in Scheme 1. In the first step, aqueous solution of Zn^{2+} and Co^{2+} ions were added dropwise to the mixed dispersion of Na-Alg, determined amount of r-GOs and melamine, where (Zn,Co)-Alg/r-GOs/melamine gels were formed. In the gels, Zn^{2+} and Co^{2+} ions are immobilized within the "egg-box" structure by coordinating with four G blocks, which is confirmed by the broad diffraction peak located at 21.0° (Fig. S1).[43] The molar ratio of Zn^{2+} to Co^{2+} is in the range of 100:1 to 3:1. Melamine can provide N source for generation of N-doped carbon. Partial of the doped N-atoms are removed through heat treatment at 900 °C and generate defects, providing anchor sites for atomic atoms.[33, 44-46] The as-prepared (Zn,Co)-Alg/r-GOs/melamine gels were dehydrated *via* a freeze-

drying process to generate (Zn,Co)-Alg/r-GOs/melamine aerogels. In the second step of pyrolysis in N_2, the metal ions are reduced *in situ* by carbonization of alginate macromolecules. At a high temperature over 800 °C, the Zn atoms were evaporated away owing to the low boiling point (mp 420 °C, bp 907 °C). The evaporation of Zn gives rise to the formation of micropores in carbon shell, providing channels for acid, thus making the sealed Co NPs easily to be dissolved by the acid. Besides, the Zn removal also generates defect sites, providing anchor sites for atomic Co. The last step of acid leaching removes the Co NPs and leaves for atomic Co species, thus forms A-Co/r-GOs. In contrast, as for aerogels without the addition of Zn, the Co NPs wrapped with dense carbon shells are not removed by acid treatment, thus forming Co NPs supported by r-GOs (Co-NP/r-GOs). In addition, it is facile to control the Co metal loading in A-Co/r-GOs by simply adjusting the molar ratio of Zn^{2+} to Co^{2+} in the first step of synthesis. It is worth to mention that the strategy is suitable for scaling up production, because the aerogels are very easy to be mass-produced.

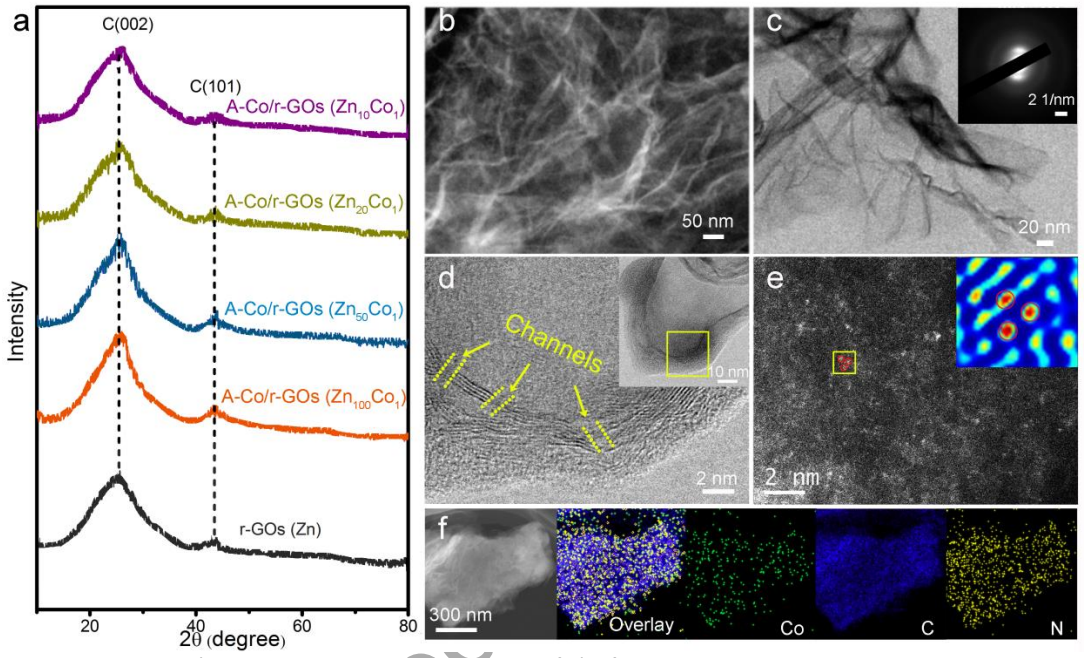

Fig. 1. (a) XRD pattern of A-Co/r-GOs prepared with different Zn^{2+}/Co^{2+} ratio (Zn_xCo_y), and r-GOs; (b) SEM image of A-Co/r-GOs ($Zn_{10}Co_1$); (c) TEM image and corresponding SAED pattern (inset) of A-Co/r-GOs ($Zn_{10}Co_1$); (d) HAADF-STEM images and enlarged images of A-Co/r-GOs ($Zn_{10}Co_1$); (e) Aberration-corrected HAADF-STEM image of A-Co/r-GOs ($Zn_{10}Co_1$) and corresponding filtered image (inset) of marked area with atomic Co atoms highlighted by red circles; (f) The EDS mapping images (overlay, Co, C, N).

The as-obtained samples were firstly studied by X-ray diffraction (XRD). As shown in Fig. S2, the samples before acid leaching display weak diffraction peaks of crystalline Co. However, after acid leaching, the XRD patterns for those samples (Fig. 1a) only exhibit diffraction peaks of (002) and (101) planes of graphitic carbon. The typical diffraction peaks of crystalline Co are not detected. In contrast, as the Zn^{2+}/Co^{2+} ratio further decreases to 3:1, a set of peaks of face-centered cubic Co exists before and even after acid leaching, which is similar with the samples without addition of Zn (Co-NP/r-GOs), indicating the formation of Co NPs (Fig. S3). To confirm the microstructure of the samples, scanning electron microscope (SEM), transmission electron microscope (TEM) and high-angle annular dark field scanning transmission electron microscope (HAADF-STEM) were performed. As shown in Fig. S4, the SEM and TEM images of A-Co/r-GOs ($Zn_{10}Co_1$) before acid leaching, Co NPs with size of ~30 nm are distributed on the graphene layers and encapsulated by graphitic carbon shell. After acid leaching, the SEM and TEM images of A-Co/r-GOs ($Zn_{10}Co_1$) are presented in Fig. 1b, 1c and S5. Obviously, there are not any Co NPs observed. The corresponding selected area electron diffraction (SAED) displays no obvious diffraction rings and spots, indicating not detectable Co (inset in Fig. 1c). The HAADF-STEM image of A-Co/r-GOs ($Zn_{10}Co_1$) indicates that only graphitic carbon shells are reserved with Co NPs removed by acid leaching (Fig. S5 and inset in Fig. 1d). The enlarged image displays that there are micropores in the graphitic carbon shells, which are generated by the evaporation of Zn. Those micro-pores provide channels for the entry of acid, enabling the acid leaching of Co NPs (Fig. 1d). Aberration-corrected HAADF-STEM reveals abundant atomically dispersed bright spots are homogeneously distributed in the carbon, which are ascribed to atomic Co owing to the different Z-contrast between Co and C (Fig. 1e and S6). The corresponding filtered image of the marked area (inset in Fig. 1e) clearly shows the atomic Co atoms (red regions), consistent with the bright spots highlighted by red circles in Fig. 1e. The corresponding mapping images indicate that Co, C, and N were distributed homogeneously over the entire architecture (Fig. 1f). The EDX analysis confirms the total removal of Zn species (Fig. S7).

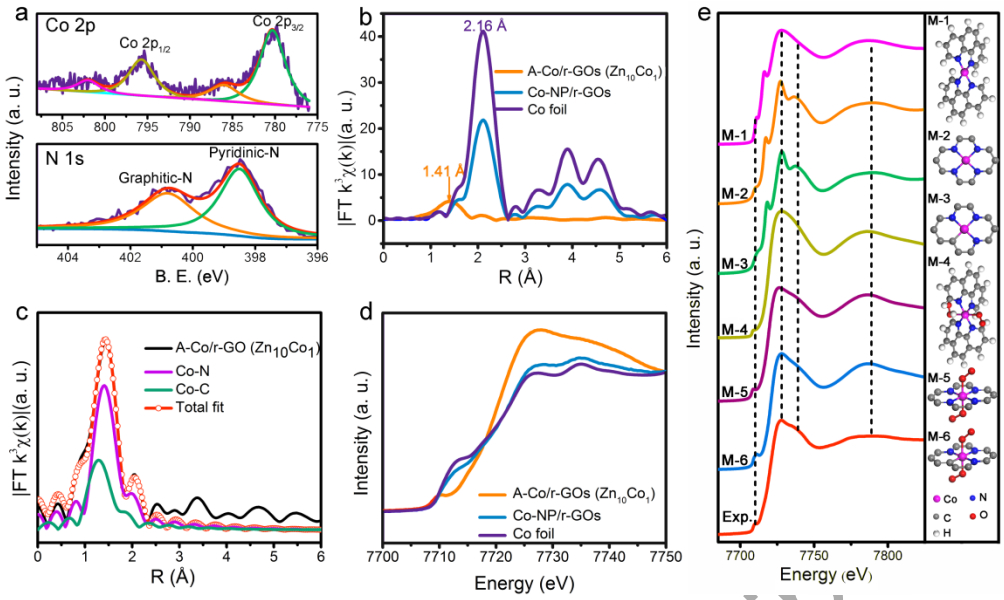

Fig. 2. (a) XPS spectra of N 1s (bottom) and Co 2p (top) of A-Co/r-GOs ($Zn_{10}Co_1$); (b) Fourier transforms of the experimental Co K-edge EXAFS spectra of the A-Co/r-GOs ($Zn_{10}Co_1$), Co-NP/r-GOs and the reference Co foil; (c) The corresponding FT-EXAFS fitting curves of A-Co/r-GOs ($Zn_{10}Co_1$); (d) Co K-edge XANES spectra of A-Co/r-GOs ($Zn_{10}Co_1$), Co foil and Co-NP/r-GOs; (e) The comparison between Co K-edge XANES experimental spectrum of A-Co/r-GOs ($Zn_{10}Co_1$) and theoretical spectrum calculated with depicted structure.

The valence state and composition of A-Co/r-GOs ($Zn_{10}Co_1$) were characterized using X-ray photoelectron spectroscopy (XPS) (Fig. S8). As revealed by the high-resolution N 1s XPS spectrum (Fig. 2a bottom), the nitrogen species are graphitic-N (400.8 eV) and pyridinic-N (398.5 eV). In addition, the binding energy of Co $2p_{3/2}$ peak is 780 eV (Fig. 2a top), which is higher than that of Co^0 (~778.5 eV), revealing the ionic nature and slight positive charge of Co species.[13, 24, 47] Raman spectroscopy was also carried out to study the structure of the samples (Fig. S9). The I_D/I_G ratios of the samples decomposed at 800, 900 and 950 °C are 0.97, 0.94 and 0.92, respectively, indicating their high graphitic quality. As described in the N_2 adsorption/desorption isotherms of r-GOs, A-Co/r-GOs ($Zn_{10}Co_1$) and Co-NP/r-GOs (Fig. S10), the absorption of micropores at a low relative pressure (P/P_0 < 0.02) increases obviously with the evaporation of Zn. This also results in the enhancement of Brunauer-Emmett-Teller (BET) surface areas with the increase of Zn^{2+}/Co^{2+} ratio (r-GOs: 425 $m^2\ g^{-1}$, A-Co/r-GOs ($Zn_{10}Co_1$): 350 $m^2\ g^{-1}$, Co-NP/r-GOs: 220 $m^2\ g^{-1}$).

Extended X-ray absorption fine structure (EXAFS) and X-ray absorption near-edge structure (XANES) measurements were performed to disclose the structure and chemical environment of Co atoms in A-Co/r-GOs ($Zn_{10}Co_1$). The Fourier transforms (FT) of EXAFS are shown in Fig. 2b. The FT-EXAFS curve of A-Co/r-GOs ($Zn_{10}Co_1$) shows a main peak at a R-space of 1.41 Å, which is much shorter than the Co-Co peak at 2.16 Å of Co foil and Co-NP/r-GOs. According to the corresponding fitting curves (Fig. 2c and S11), the main peak can be attributed to the backscattering between Co and N/C.[13] The minor satellite peak at 2.0~2.3 Å has also been observed in previous atomic materials, which is interpreted as Co-N/C contributions.[46] According to the fitting parameters, the coordination numbers of the N and C atoms are estimated to be 2.8 and 1.2, respectively (Table S1). The electronic structure of Co is indicated by the X-ray absorption near-edge structure (XANES) analysis (Fig. 2d). The white line peak intensity for A-Co/r-GOs ($Zn_{10}Co_1$) is obviously higher than that of Co-NP/r-GOs and Co foil, confirming the oxidized electronic structure of the atomic Co.[11, 13, 48, 49] This observation agrees well with the aforementioned XPS results and reported literatures.[13, 48] The XANES was also used to determine the structure configuration of the A-Co/r-GOs ($Zn_{10}Co_1$) due to its high sensitivity to the arrangement of atoms around the photo-absorber.[48, 50] The absence of pre-edge peak at 7714–7716 eV, which is assigned to a $1s \rightarrow 4p_z$ shakedown transition characteristic for a square-planar configuration with high D_{4h} symmetry, indicates that it is not a planar structure and calls for axial ligands.[51, 52] The XANES simulations of various density functional theory (DFT)-optimized architectural models (M-1 to M-6) were performed (Fig. 2e). It is found that M-6 could best reproduce all the features of the experimental spectra, that is, the CoN_3C moiety enclosed in a graphene plane with two axial oxygen molecules absorbed end-on.[24, 49, 53]

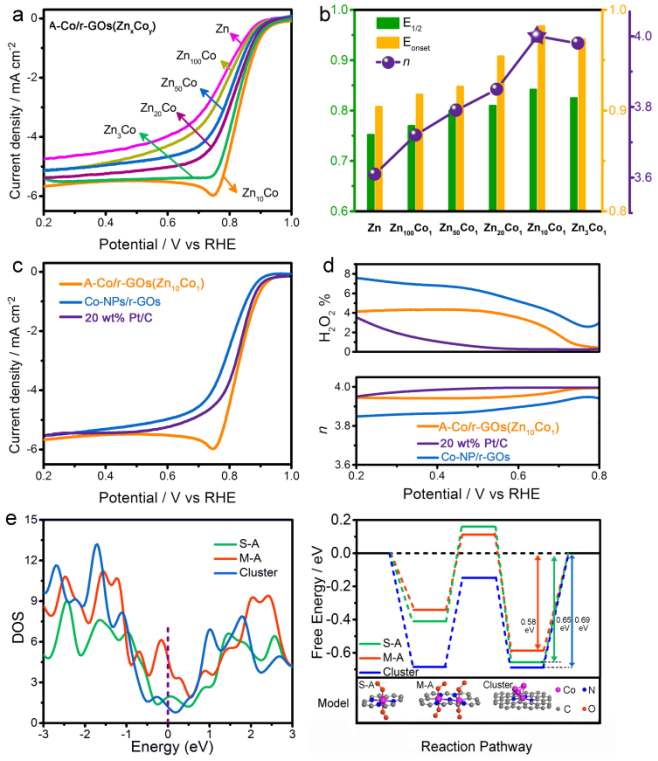

Fig. 3. (a) LSV curves of A-Co/r-GOs decomposed at 900 °C with different Zn/Co ratio; (b) Comparison of E_{onset} (E_{onset} was acquired at a ORR current density of −0.1 mA cm^{-2}), $E_{1/2}$ and electron transfer number for different catalysts; LSV curves (c), and electron transfer number (n) and H_2O_2 yield (d) of A-Co/r-GOs ($Zn_{10}Co_1$), Co-NPs/r-GOs and 20 wt. % Pt/C; (e) Total electronic density of states (DOS) for S-A, M-A and cluster (the Fermi energy level EF was set to zero); (f) Free energy diagram for the ORR pathway for S-A, M-A and cluster under alkaline conditions at the equilibrium potential of U_0=0.461 V.

More importantly, this synthetic methodology is universal for other atomic metal catalysts. For example, atomic Cu and Ni were also successfully synthesized using this strategy. As shown in Fig. S12, no typical diffraction peaks of crystalline Cu/Ni are detected from the XRD patterns of both A-Cu/r-GOs and A-Ni/r-GOs. Their HAADF-STEM images display abundant bright spots, which are ascribed to atomic Cu and Ni (Fig.S13). The XPS measurements are used to disclose the valence state and composition of A-Cu/r-GOs and A-Ni/r-GOs (Fig. S14 and **S15**). The binding energy of Cu $2p_{3/2}$ and Ni $2p_{3/2}$ peak are 934.3 and 854.7 eV, respectively, which is higher than that of Cu^0 (~932.6 eV) and Ni^0 (~852.5 eV), revealing a slight positive charge due to N/C-coordination.[24, 54] XANES and EXAFS measurements are measured to confirm the atomically dispersed state of Cu and Ni atoms. The higher white line peak intensity of A-Cu/r-GOs and A-Ni/r-GOs than those of Cu/Ni foil confirms the oxidized electronic structure of atomic Cu/Ni, which is consistent with the results of XPS (Fig. S16a and c). The main peaks of FT-EXAFS for A-Cu/r-GOs and A-Ni/r-GOs locate at 1.40 and 1.42 Å, which are ascribed to the backscattering between metal and light atoms (Fig. S16b and d). Together with the deficiency of Cu-Cu and Ni-Ni paths, the atomically dispersed Cu and Ni atoms could be corroborated.

The catalytic activities for ORR of the samples were studied by the linear sweep voltammetry (LSV) with a rotating disk electrode (RDE) in O_2-saturated 0.1 M KOH. The superior ORR activity of A-Co/r-GOs to that of r-GOs (without addition of Co) demonstrates the atomic Co species are indeed of great significance in enhancing the catalytic performance (Fig. 3a). Obviously, the decrease of Zn/Co ratio positively shifts the polarization curves. This is because that the Co metal loading increases with the decrease of Zn/Co ratio, which significantly boosts the accessible active sites. The A-Co/r-GOs ($Zn_{10}Co_1$) achieves the best ORR activity, as judged by the onset (E_{onset} = 0.984 V vs. RHE) and half-wave ($E_{1/2}$ = 0.842 V vs. RHE) potential in Fig. 3b. The Co metal loading of A-Co/r-GOs ($Zn_{10}Co_1$) is 3.6 wt. % as indicated by the thermogravimetric analysis (Fig. S17). However, the ORR activity declines when the Zn/Co ratio is further decreased to 3:1, which is indicated by the slightly negative E_{onset} (0.974 V vs. RHE) and $E_{1/2}$ (0.825 V vs. RHE). The degradation of catalytic performance can be attributed to the decreasing numbers of accessible active sites caused by the partially aggregation of atomic Co. The value of electron transfer numbers (n) for those samples calculated based on Koutecky-Levich (K-L) equation are 3.61 (r-GOs), 3.72 ($Zn_{100}Co_1$), 3.79 ($Zn_{50}Co_1$), 3.85 ($Zn_{20}Co_1$), 4.0 ($Zn_{10}Co_1$), 3.98 (Zn_3Co_1), respectively (Fig. S20). Obviously, the electron transfer rate of those catalysts is gradually enhanced with the increase of Co metal loading, indicating improved ORR activity. Furthermore, compared with Co-NP/r-GOs and the commercial 20 wt% Pt/C (Fig. 3c**)**, the $E_{1/2}$ of A-Co/r-GOs ($Zn_{10}Co_1$) is 15 mV and 50 mV more positive than that of 20 wt% Pt/C ($E_{1/2}$ of 0.827 V vs. RHE) and Co-NP/r-GOs (0.792V vs. RHE), respectively. The RRDE technique was also performed to monitor the generation of H_2O_2 and determine the n value. As revealed in Fig. 3d, the H_2O_2 yield of A-Co/r-GOs ($Zn_{10}Co_1$) remains below 4.3 % with the n value ranging from 3.92 to 4.0 over the potential range of 0.2−0.8 V vs. RHE, similar to that of 20 wt% Pt/C. These results confirm the direct four-electron pathway over A-Co/r-GOs ($Zn_{10}Co_1$), demonstrating its high ORR catalytic efficiency. The detailed LSV curves, K-L plots and electron transfer numbers for the samples with different Co metal loading, r-GOs contents and pyrolysis temperatures are presented in Fig. S20-22. To better clarify the effect of acid leaching, the samples before acid leaching were tested (Figure S23). The Tafel slope of A-Co/r-GOs ($Zn_{10}Co_1$) (67 mV dec^{-1}) is much lower than that of the sample before acid leaching (88 mV dec^{-1}), indicating that acid leaching makes A-Co/r-GOs faster kinetics (Figure S24). We also tested the ORR performances of A-Co/r-GOs in 0.5 M H_2SO_4 (Fig. S25). The half-wave potential ($E_{1/2}$) of A-Co/r-GOs is about 0.71 V vs. RHE, which is very close to that in the previous literatures in aspects of $E_{1/2}$ (−0.75~−0.85 V). Besides the activity, stability is another important parameter for high-performance electrocatalysts for practical applications. The electrochemical stability of A-Co/r-GOs ($Zn_{10}Co_1$) was assessed by cycling between 0.6 and 1.0 V at 50 mV s^{-1}. As shown in Fig. S18a, no obvious change in $E_{1/2}$ and E_{onset} is observed after 5000 cycles. Also, the A-Co/r-GOs ($Zn_{10}Co_1$) exhibits a slower decrease and less current loss (11%) than that of Pt/C (22%) as indicated by the current-time (i-t) chronoamperometric response (Fig. S18b),

demonstrating its super stability. After stability test, abundant atomically dispersed bright spots are observed from the HAADF-STEM image (Fig. S19). This means these Co atoms are homogeneously distributed in the carbon without aggregation, demonstrating the great stability of single Co sites.

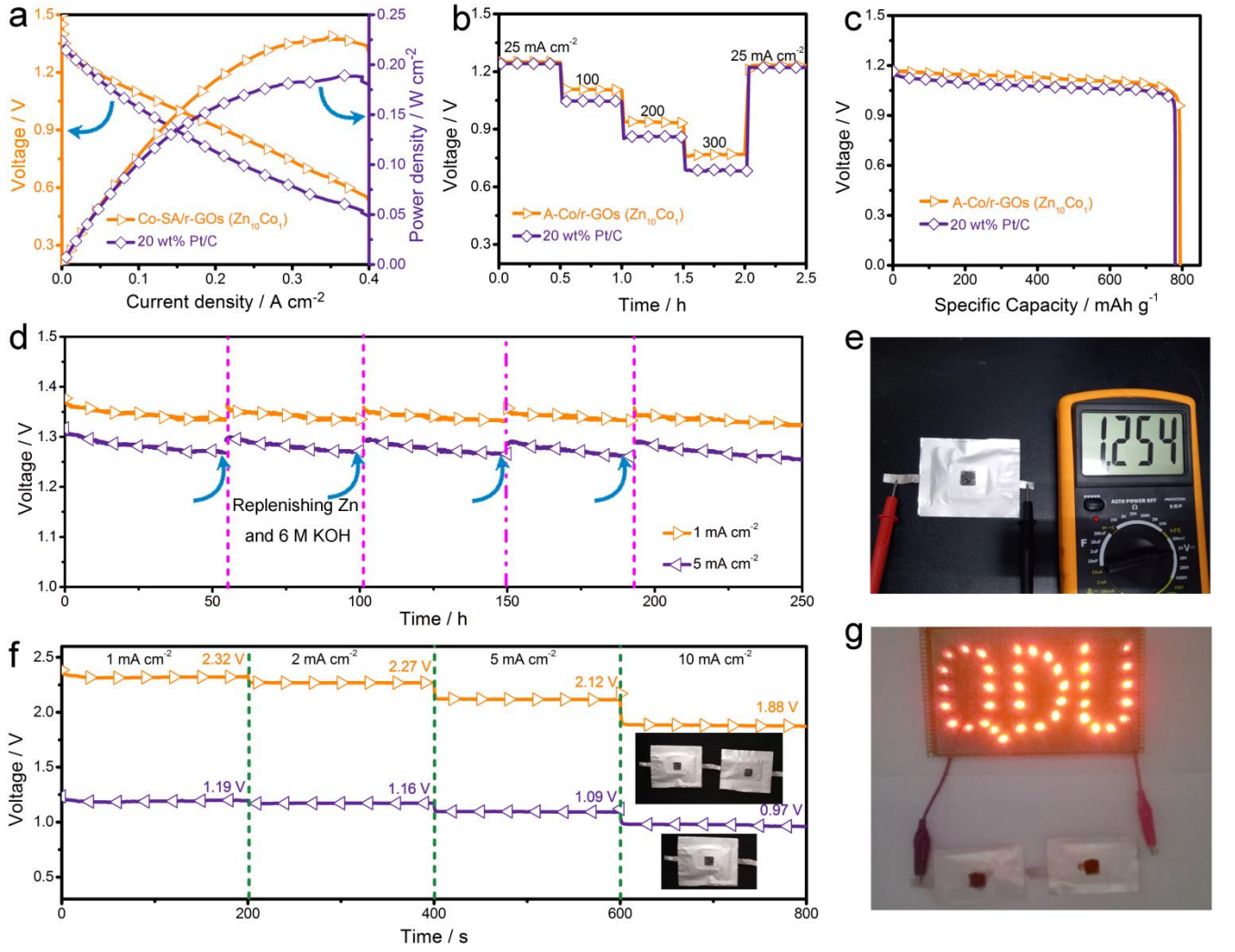

Fig. 4. (a) The discharge polarization curves and corresponding power density plots of ZABs driven by A-Co/r-GOs ($Zn_{10}Co_1$) and commercial Pt/C; (b) Discharge curves of the ZABs from low current densities to high current densities (25, 100, 200, 300 mA cm^{-2}); (c) Specific capacities normalized to the mass of the consumed zinc of the ZABs at current density of 50 mA cm^{-2}; (d) Mechanically recharged A-Co/r-GOs-based ZABs at 1 and 5 mA cm^{-2} in ambient air conditions; (e) Photograph of an all-solid-state ZABs with an open circuit voltage of 1.25 V; (f) Galvanostatic discharge curves of one and two all-solid-state ZABs in series at different current densities (1, 2, 5 and 10 mA cm^{-2}), respectively; (h) Photographs of red LED panel powered by two all-solid-state ZABs in series.

We performed the first principles to further investigate the superior ORR performance of A-Co/r-GOs. As depicted in the bottom of Fig. 3d, the single atomic Co (S-A), multi-atomic Co (M-A) and cluster based on M-6 configuration were built to illustrate the experimental results. Density of state (DOS) was calculated to analyze charge-transfer ability and electronic conductivity. As shown in Fig. 3e, the DOS of S-A, M-A and cluster around the Fermi level is consecutive without any gap, demonstrating their metallic characters.[38, 55, 56] Moreover, the DOS near the Fermi level of M-A is more intense than that of S-A and cluster, indicating that M-A is more metal-like with better charge-transfer efficiency and conductivity.[57, 58] It suggests that the electrical property of A-Co/r-GOs can be improved when the number of atomic Co is increased. The Gibbs free energy (ΔG) of intermediates was computed to illuminate the reaction pathways and the catalytic activity. Three intermediates, OOH*, O*, and OH* (with the asterisk denoting the adsorption site) are generated with stepwise addition of H_2O and electrons to form OH^-.[59] The ΔG of intermediates on cluster is much more negative than those of S-A and M-A, indicating the strong chemisorption of oxygen species on cluster.[52] However, in the last step for desorption of OH*, a reaction barrier of 0.69 eV is presented as the overall rate-limiting step. In case of S-A and M-A, the last step is also the overall rate-limiting step in the oxygen

reduction pathway. Alternatively, multi-SA exhibits the lowest reaction barrier of 0.58 eV, indicating M-A is of the highest catalytic activities for ORR. The DFT calculations suggest that the ORR catalytic performance of atomically dispersion catalysts can be efficiently improved by increasing the metal loading (e.g. decreasing the distance of the Co and Co atoms), which is in agreement with our experimental results.

ZABs are suffered from their low power-output capability, which is caused by the low efficiency of air cathode. The A-Co/r-GOs can accelerate the ORR rate, thus it is expected to improve the air cathode efficiency, then enhance the battery performance. To further investigate the potential application in ZABs, the ORR performance of A-Co/r-GOs ($Zn_{10}Co_1$) and 20 wt% Pt/C in O_2-saturated 6 M KOH solution was evaluated (Fig. S26). Due to the decreased oxygen solubility and diffusion coefficient, and increased viscosity, the limiting current density in 6 M KOH solution greatly decreases compared to that in 0.1 M KOH solution. Obviously, the A-Co/r-GOs ($Zn_{10}Co_1$) exhibits a more positive half-wave potential than that of 20 wt% Pt/C. Then primary aqueous ZABs with A-Co/r-GOs ($Zn_{10}Co_1$) loaded on carbon paper and a polished Zn plate as the air cathode and anode, respectively, were assembled to demonstrate the potential use for real energy device of our catalyst (Fig. S27). For a direct comparison, the ZAB made of the commercial 20 wt% Pt/C catalyst was also fabricated and tested under the same conditions. Fig. 4a shows the polarization curves and corresponding power density of A-Co/r-GOs- and Pt/C-based ZABs. The A-Co/r-GOs-based ZABs deliver a current density of ~ 153.4 mA cm^{-2} at a voltage of 1.0 V and maximum peak power density of ~ 0.225 W cm^{-2} at 0.668 V, which are obviously superior to those of Pt/C-based ZABs (~ 106 mA cm^{-2} and 0.188 W cm^{-2}) and most of the reported electrocatalysts (Table S2). Moreover, the A-Co/r-GOs-based-ZABs also demonstrate outstanding current set up and down response characteristics, indicating their potential automobile application, which need fast dynamic response (Fig. 4b). The A-Co/r-GOs-based ZABs display potential plateaus of 1.25, 1.11, 0.94 and 0.77 V at discharge current densities of 25, 100, 200 and 300 mA cm^{-2}, respectively, which are obviously higher than those of Pt/C-based ZABs. The results are consistent with the discharge polarization. The capacity of a ZAB is obtained by a full-discharge experiment in which the zinc foils were exhausted (Fig. 4c). Normalized to the mass of consumed zinc, the specific capacity of A-Co/r-GOs ($Zn_{10}Co_1$)-based ZABs reaches ~ 795 mAh g_{zn}^{-1}, corresponding to a gravimetric energy density of ~ 805 Wh kg^{-1}, which are better than those of Pt/C-based ZABs (~ 778 mAh g^{-1} and ~ 775 Wh kg^{-1}, respectively). Besides high discharge voltage and specific zinc capacity, the air cathodes catalyzed by A-Co/r-GOs ($Zn_{10}Co_1$) were demonstrated with superb stability. As shown in Fig. S28, obviously, after galvanostatically discharged for 50 h, the A-Co/r-GOs ($Zn_{10}Co_1$)-based ZABs exhibit much less voltage losses than those of Pt/C-based ZABs. Notably, the air cathode catalyzed by A-Co/r-GOs ($Zn_{10}Co_1$) could work robustly for more than 250 h with little voltage loss by replenishing the Zn plate and electrolyte periodically (Fig. 4d). What's more, after fully discharged, the ZABs can be recharged by refueling the Zn plate and electrolyte with negligible voltage loss, attesting again the superb durability of the catalyst (Fig. S29). The excellent stability of A-Co/r-GOs ($Zn_{10}Co_1$)-based ZABs can be attributed to the superior ORR stability of A-Co/r-GOs ($Zn_{10}Co_1$). Apart from the aqueous ZABs, all-solid-state ZABs were also fabricated with A-Co/r-GOs ($Zn_{10}Co_1$) loaded on Ni foam as air cathode, a polished Zn plate as anode, and alkaline poly(vinyl alcohol) (PVA) as the gel electrolyte to demonstrate its potential applications in our daily life devices. As shown in Fig. 4e, an all-solid-state ZAB displays an open circuit voltage of 1.25 V. Fig. 4f depicts the galvanostatic discharge curves of the all-solid-state ZABs. Two ZABs in series exhibit discharging voltages of 2.32 V, 2.27 V. 2.12 V and 1.88 V at discharge current densities of 1, 2, 5 and 10 mA cm^{-2}, respectively, which are almost twice times the voltage of a single ZAB under the same conditions. This demonstrates a viable way to extend the output voltage. Finally, as a demo, two all-solid-state ZABs in series is capable of lighting a red LED panel with a rated voltage of 2 V (Fig. 4g).

Conclusions

In summary, we reported a general, scalable and controllable strategy to synthesize atomically dispersed metal on reduced graphene oxides (A-M/r-GOs) with the assistance of "egg-box" in alginate. The central synthesis is based on the "egg-box" structure in alginate, where each metal cations (M^{2+} and Zn^{2+}) is confined in the "egg-box". The evaporation of Zn on one hand generates pores, providing channels for acid entrance, and on the other hand, provides defects as anchor sites for atomic Co species. The as synthesized A-Co/r-GOs with a maximum metal loading of 3.6 wt. % exhibits superior ORR catalytic activity and stability. Besides, the catalyst achieves superior performance as an air cathode for primary ZABs. The A-Co/r-GOs ($Zn_{10}Co_1$)-based air cathode could work robustly for more than 250 h by replenishing the Zn plate and electrolyte periodically. Given the low-cost and eco-friendly nature of Na-Alg (~ 5 $/kg), this work really offers a realistic methodology for scalable and cost-effective synthesis of high-efficiency atomically dispersed metal electrocatalysts with a high loading.

Acknowledgements

We are grateful for the financial support by the National Natural Science Foundation of China (grant no. 51473081 and 51672143), Outstanding Youth of Natural Science in Shandong Province (JQ201713), Taishan Scholars Program and ARC Discovery Project (No. 170103317).

Notes and references

1 X.-F. Yang, A. Wang, B. Qiao, J. Li, J. Liu, T. Zhang, Acc. Chem. Res. 2013, **46**, 1740.
2 E. J. Peterson, A. T. DeLaRiva, S. Lin, R. S. Johnson, H. Guo, J. T. Miller, J. Hun Kwak, C. H. Peden, B. Kiefer, L. F. Allard, F. H. Ribeiro, A. K. Datye, Nature Commun. 2014, **5**, 4885.

3 B. Qiao, A. Wang, X. Yang, L. F. Allard, Z. Jiang, Y. Cui, J. Liu, J. Li, T. Zhang, Nature Chem. 2011, **3**, 634.
4 Y. Cao, S. Chen, Q. Luo, H. Yan, Y. Lin, W. Liu, L. Cao, J. Lu, J. Yang, T. Yao, S. Wei, Angew. Chem. Int. Ed. 2017, **56**, 12191.
5 G. Gao, Y. Jiao, E. R. Waclawik, A. Du, J. Am. Chem. Soc. 2016, **138**, 6292.
6 X. Guo, G. Fang, G. Li, H. Ma, H. Fan, L. Yu, C. Ma, X. Wu, D. Deng, M. Wei, D. Tan, R. Si, S. Zhang, J. Li, L. Sun, Z. Tang, X. Pan, X. Bao, Science 2014, **344**, 616.
7 G. Liu, A. W. Robertson, M.-J. Li, W. C. H. Kuo, M. T. Darby, M. H. Muhieddine, Y.-C. Lin, K. Suenaga, M. Stamatakis, J. H. Warner, S. C. E. Tsang, Nat. Chem. 2017, **9**, 810.
8 H. Yan, H. Cheng, H. Yi, Y. Lin, T. Yao, C. Wang, J. Li, S. Wei, J. Lu, J. Am. Chem. Soc.y 2015, **137**, 10484.
9 H. Wei, X. Liu, A. Wang, L. Zhang, B. Qiao, X. Yang, Y. Huang, S. Miao, J. Liu, T. Zhang, Nature Commun. 2014, **5**, 5634.
10 S. Back, J. Lim, N. Y. Kim, Y. H. Kim, Y. Jung, Chem. Sci. 2017, 8, 1090.
11 G. Gao, Y. Jiao, E. R. Waclawik, A. Du, J. Am. Chem. Soc. 2016, 138, 6292.
12 H. Fei, J. Dong, M. J. Arellano-Jimenez, G. Ye, N. Dong Kim, E. L. Samuel, Z. Peng, Z. Zhu, F. Qin, J. Bao, M. J. Yacaman, P. M. Ajayan, D. Chen, J. M. Tour, Nature Commun. 2015, **6**, 8668.
13 N. Tian, Z.-Y. Zho S.-G. Sun, Y. Ding, Z. L. Wang, Science, 2007, **316**, 732.
14 P. Yin, T. Yao, Y. Wu, L. Zheng, Y. Lin, W. Liu, H. Ju, J. Zhu, X. Hong, Z. Deng, G. Zhou, S. Wei, Y. Li, Angew. Chem. 2016, **55**, 10800.
15 P. Chen, T. Zhou, L. Xing, K. Xu, Y. Tong, H. Xie, L. Zhang, W. Yan, W. Chu, C. Wu, Y. Xie, Angew. Chem. Int. Ed, 2017, **56**, 610.
16 A. Cuesta, ChemPhysChem 2011, **12**, 2375.
17 S. Stambula, N. Gauquelin, M. Bugnet, S. Gorantla, S. Turner, S. Sun, J. Liu, G. Zhang, X. Sun, G. A. Botton, J. Phys. Chem. C 2014, **118**, 3890.
18 N. Cheng, S. Stambula, D. Wang, M. N. Banis, J. Liu, A. Riese, B. Xiao, R. Li, T. K. Sham, L. M. Liu, G. A. Botton, X. Sun, Nature Commun. 2016, **7**, 13638.
19 G. Kyriakou, M. B. Boucher, A. D. Jewell, E. A. Lewis, T. J. Lawton, A. E. Baber, H. L. Tierney, M. F.-Stephanopoulos, E. C. H. Sykes, Science 2012, **335**, 1209.
20 J. Lin, A. Wang, B. Qiao, X. Liu, X. Yang, X. Wang, J. Liang, J. Li, J. Liu, T. Zhang, J. Am. Chem. Soc. 2013, **135**, 15314.
21 S. Yang, J. Kim, Y. J. Tak, A. Soon, H. Lee, Angew. Chem. Int. Ed. 2016, **55**, 2058.
22 S. Abbet, A. Sanchez, U. Heiz, W.-D. Schneider, A. M. Ferrari, G. Pacchioni, N. Rösch, J. Am. Chem. Soc. 2000, **122**, 3453.
23 X. Zhang, J. Guo, P. Guan, G. Qin, S. J. Pennycook, Phys. Rev. Lett. 2015, **115**, 147601.
24 S. Sun, G. Zhang, N. Gauquelin, N. Chen, J. Zhou, S. Yang, W. Chen, X. Meng, D. Geng, M. N. Banis, R. Li, S. Ye, S. Knights, G. A. Botton, T.-K. Sham, X. Sun, Sci. Rep. 2013, **3**, 1775.
25 C. Zhao, X. Dai, T. Yao, W. Chen, X. Wang, J. Wang, J. Yang, S. Wei, Y. Wu, Y. Li, J. Am. Chem. Soc. 2017, **139**, 8078.
26 Y. Chen, S. Ji, Y. Wang, J. Dong, W. Chen, Z. Li, R. Shen, L. Zheng, Z. Zhuang, D. Wang, Y. Li, Angew. Chem. Int. Ed. 2017, **56**, 6937.
27 B. Wang, X. Wang, J. Zou, Y. Yan, S. Xie, G. Hu, Y. Li, A. Dong, Nano letters 2017, **17**, 2003.
28 T. Xu, D. Li, S. Chen, Y. Sun, H. Zhang, Y. Xia, D. Yang, Chem. Eng. J., 2018, 345, 604.
29 L. Liu, X. Yang, N. Ma, H. Liu, Y. Xia, C. Chen, D. Yang, X. Yao, Small 2016, **12**, 1295.
30 Z. Wei, Y. Chen, J. Wang, D. Su, M. Tang, S. Mao, Y. Wang, ACS Catalysis 2016, **6**, 5816.
31 M. Zeng, Y. Liu, F. Zhao, K. Nie, N. Han, X. Wang, W. Huang, X. Song, J. Zhong, Y. Li, Adv. Funct. Mater. 2016, **26**, 4397.
32 L. Fan, P. F. Liu, X. Yan, L. Gu, Z. Z. Yang, H. G. Yang, S. Qiu, X. Yao, Nature Commun. 2016, **7**, 10667.
33 X. Zhao, X. Zou, X. Yan, C. L. Brown, Z. Chen, G. Zhu, X. Yao, Inorg. Chem. Front. 2016, **3**, 417.
34 L. Zhang, Y. Jia, G. Gao, X. Yan, N. Chen, J. Chen, M. T. Soo, B. Wood, D. Yang, A. Du, X. Yao, Chem. 2018, **4**, 1.
35 Y. Gu, S. Chen, J. Ren, Y. A. Jia, C. Chen, S. Komarneni, D. Yang, X. Yao, ACS Nano 2018, **12**, 245.
36 N. Ma, Y. Jia, X. Yang, X. She, L. Zhang, Z. Peng, X. Yao, D. Yang, J. Mater. Chem. A 2016, **4**, 6376.
37 J. Sun, C. Lv, F. Lv, S. Chen, D. Li, Z. Guo, W. Han, D. Yang, S. Guo, ACS Nano 2017, **11**, 6186.
38 D. Li, D. Yang, X. Yang, Y. Wang, Z. Guo, Y. Xia, S. Sun, S. Guo, Angew. Chem. Int. Ed. 2017, **55**, 15925.
39 Y. Zou, G. Chang, S. Chen, T. Liu, Y. Xia, C. Chen, D. Yang, Chem. Eng. J., 2018, 351, 340.
40 Y. Zou, X. Yang, C. Lv, T. Liu, Y. Xia, L. Shang, G. I. N. Waterhouse, D. Yang, T. Zhang, Adv. Sci. 2017, **4**, 1600262.
41 Y. Zou, S. Chen, X. Yang, N. Ma, Y. Xia, D. Yang, S. Guo, Adv. Energy Mater. 2016, **6**, 1601549.
42 Y. Zou, G. Chang, Y. Jia, R. Cai, S. Chen, Y. Xia, W. Theis, D. Yang, X.Yao, Energy Storage Materials, 2018, **15**, 202.
43 Y. Jia, L. Zhang, A. Du, G. Gao, J. Chen, X. Yan, C. L. Brown, X. Yao, Adv. Mater. 2016, **28**, 9532.
44 X. Yan, Y. Jia, T. Odedairo, X. Zhao, Z. Jin, Z. Zhu, X. Yao, Chem. Commun. 2016, **52**, 8156.
45 H. Fei, J. Dong, Y. Feng, C. S. Allen, C. Wan, B. Volosskiy, M. Li, Z. Zhao, Y. Wang, H. Sun, P. An, W. Chen, Z. Guo, C. Lee, D. Chen, I. Shakir, M. Liu, T. Hu, Y. Li, A. I. Kirkland, X. Duan, Y. Huang, Nature Catalysis 2018, **1**, 63.
46 Li, D. Y. Jia, G. Chang, J. Chen, H. Liu, J. Wang, Y. Hu,Y. Xia, D. Yang, X. Yao, Chem, doi: org/10.1016/j.chempr.2018.07.005.
47 W. Liu, L. Zhang, W. Yan, X. Liu, X. Yang, S. Miao, W. Wang, A. Wang, T. Zhang, Chem. Sci. 2016, **7**, 5758.
48 Y. Cao, S. Chen, Q. Luo, H. Yan, Y. Lin, W. Liu, L. Cao, J. Lu, J. Yang, T. Yao, S. Wei, Angew. Chem. Int. Ed. 2017, **56**, 12191.
49 A. Zitolo, N. Ranjbar-Sahraie, T. Mineva, J. Li, Q. Jia, S. Stamatin, G. F. Harrington, S. M. Lyth, P. Krtil, S. Mukerjee, E. Fonda, F. Jaouen, Nature Commun. 2017, **8**, 957.
50 J. Wang, Z. Huang, W. Liu, C. Chang, H. Tang, Z. Li, W. Chen, C. Jia, T. Yao, S. Wei, Y. Wu, Y. Li, J. Am. Chem. Soc. 2017, **139**, 17281.
51 T. E. Westre, P. Kennepohl, J. G. DeWitt, B. Hedman, K. O. Hodgson, E. I. Solomon, J. Am. Chem. Soc. 1997, **119**, 6297.
52 C. Zhang, J. Sha, H. Fei, M. Liu, S. Yazdi, J. Zhang, Q. Zhong, X. Zou, N. Zhao, H. Yu, Z. Jiang, E. Ringe, B. I. Yakobson, J. Dong, D. Chen, J. M. Tour, ACS Nano 2017, **11**, 6930.
53 A. Zitolo, V. Goellner, V. Armel, M.-T. Sougrati, T. Mineva, L. Stievano, E. Fonda, F. Jaouen, Nature Mater. 2015, **14**, 937.
54 J. Li, N. Zhou, J. Song, L. Fu, J. Yan, Y. Tang, H. Wang, ACS Sustainable Chem. Eng. 2017, **6**, 413-421.
55 K. Xu, P. Chen, X. Li, Y. Tong, H. Ding, X. Wu, W. Chu, Z. Peng, C. Wu, Y. Xie, J. Am. Chem. Soc. 2015, **137**, 4119.
56 D. Gao, J. Zhang, T. Wang, W. Xiao, K. Tao, D. Xue, J. Ding, J. Mater. Chem. A 2016, **4**, 17363.
57 Y. Zhao, X. Jia, G. Chen, L. Shang, G. I. Waterhouse, L. Z. Wu, C. H. Tung, D. O'Hare, T. Zhang, J. Am. Chem. Soc. 2016, **138**, 6517.
58 W. Chen, J. Pei, C. T. He, J. Wan, H. Ren, Y. Zhu, Y. Wang, J. Dong, S. Tian, W. C. Cheong, S. Lu, L. Zheng, X. Zheng, W. Yan, Z. Zhuang, C. Chen, Q. Peng, D. Wang, Y. Li, Angew. Chem. Int. Ed. 2017, **56**, 16086.
59 Y. Jiao, Y. Zheng, M. Jaroniec, S. Z. Qiao, J. Am. Chem. Soc. 2014, 136, 4394.

